

Computational imaging through a fiber-optic bundle

Muhammad A. Lodhi^a, John Paul Dumas^b, Mark C. Pierce^b, and Waheed U. Bajwa^a

^aDepartment of Electrical and Computer Engineering, Rutgers University

^bDepartment of Biomedical Engineering, Rutgers University

ABSTRACT

Compressive sensing (CS) has proven to be a viable method for reconstructing high-resolution signals using low-resolution measurements. Integrating CS principles into an optical system allows for higher-resolution imaging using lower-resolution sensor arrays. In contrast to prior works on CS-based imaging, our focus in this paper is on imaging through fiber-optic bundles, in which manufacturing constraints limit individual fiber spacing to around $2\text{ }\mu\text{m}$. This limitation essentially renders fiber-optic bundles as low-resolution sensors with relatively few resolvable points per unit area. These fiber bundles are often used in minimally invasive medical instruments for viewing tissue at macro and microscopic levels. While the compact nature and flexibility of fiber bundles allow for excellent tissue access *in-vivo*, imaging through fiber bundles does not provide the fine details of tissue features that is demanded in some medical situations. Our hypothesis is that adapting existing CS principles to fiber bundle-based optical systems will overcome the resolution limitation inherent in fiber-bundle imaging. In a previous paper we examined the practical challenges involved in implementing a highly parallel version of the single-pixel camera while focusing on synthetic objects. This paper extends the same architecture for fiber-bundle imaging under incoherent illumination and addresses some practical issues associated with imaging physical objects. Additionally, we model the optical non-idealities in the system to get lower modelling errors.

1. INTRODUCTION

Endoscopy is a technique of particular interest in the medical imaging community as it allows for *in-vivo* access to tissues for minimally invasive surgeries. Coherent fiber-optic bundles are commonly used in endoscopy because they are compact, flexible, and provide ample light throughput for imaging purposes. While these qualities are favorable for clinical use, traditional fiber bundle imaging is unable to provide the histopathology-level resolution that is required for some applications. It is technically challenging to fabricate bundles with small, densely packed fibers to achieve a high number of resolvable points in a given field of view. As a result, imaging through a fiber bundle results in loss of fine details when compared to microscopy (Fig. 1). Furthermore, core-to-core coupling, or crosstalk, increases with closer fiber spacing, particularly at near-infrared wavelengths.¹ A new strategy, therefore, is needed to overcome this resolution limitation of fiber-bundle imaging without increasing the outer diameter of an endoscopic probe.

To overcome the resolution limitation of fiber-bundle imaging, while modifying the physical platform as little as possible, we direct our focus towards compressive sensing (CS).^{2–6} The principles of CS provide a theoretical framework that enables one to reconstruct a signal that is sparse in some domain from much fewer samples than dictated by the traditional Nyquist sampling theorem. When integrated into an optical imaging system, where images are often sparse in wavelet or other domains, CS techniques make it possible to generate images with more resolvable points than are physically present in an optical sensor, such as a camera. Our goal in this paper is to demonstrate that assimilating CS into endoscopic imaging can help overcome the resolution limitations incurred by fiber-optic bundles. Integrating CS for our proposed computational endomicroscopy approach involves the addition of a coded mask at the distal end of a traditional setup which contains more elements than there are fibers in the bundle. CS reconstruction algorithms then contend that several diverse low-resolution observations of a scene through different masks can be used to obtain a single high-resolution image with more resolvable points than there are fibers in the bundle.

Further author information: (Send correspondence to M.A.L.)

M.A.L.: masad.lodhi@rutgers.edu, **W.U.B.:** waheed.bajwa@rutgers.edu

J.P.D.: jd1051@scarletmail.rutgers.edu, **M.P.:** mp941@soe.rutgers.edu

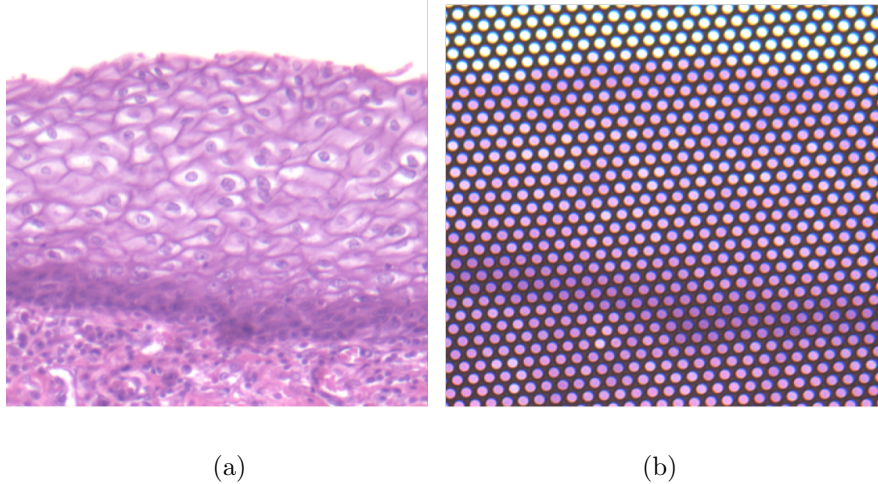


Figure 1. The same region of an Haemotoxylin & Eosin stained tissue slide imaged (a) with a microscope and (b) through a fiber bundle.

In terms of relationship to prior work, imaging systems based on CS principles are common in the existing literature.^{7–16} A prototypical example of such a system is the Rice Single-Pixel Camera,⁷ which demonstrates the extreme case of CS by imaging a scene using a single photodetector, or pixel. To generate a high resolution image, several measurements of a static scene are recorded, each through a different mask. Afterwards CS algorithms are used to reconstruct an image with more pixels than there were individual sensors. The single-pixel camera sparked interest into integrating CS into imaging modalities and currently there are several architectures that exploit these principles. Various modifications of the single pixel camera have been proposed to reduce the sampling time by taking several measurements in parallel by using sensor arrays.^{8–11} Other architectures that differ on the type and location of the mask have also been proposed.^{12–16} However, none of the aforementioned systems investigate imaging through the fiber bundles and the ones that actually deal with fiber bundles do not exploit the CS principles.

In this paper, we take the first step towards integrating CS principles into endoscopy imaging by proposing an architecture for computational imaging through fiber bundles and putting forth a preliminary forward model for this architecture. We also investigate the performance of our proposed architecture and model using both numerical and a physical experimental setup (see Sec. 5). Our numerical simulations explore fiber bundles of different radii with regular or irregular arrangement of fibers in the bundle. Additionally, we discuss how to learn and incorporate imperfections of the imaging system in our forward model to obtain better reconstructions.

The organization of the rest of the paper is as follows: In Sec. 2 we describe the limitations of the conventional fiber-bundle imaging setup. Then in Sec. 3 we put forth the CS-based modified setup for fiber bundle imaging and provide a forward model for this setup. In Sec. 4 and 5 we provide results for numerical experiments for data collected from an experimental platform. And in Sec. 6 we conclude our paper.

2. LIMITATIONS OF TRADITIONAL FIBER-BUNDLE IMAGING AND PROPOSED ALTERNATIVE

In this section, we will motivate the need for computational imaging through fiber-optic bundles and the challenges that it entails. In the traditional fiber-bundle imaging setup, the object is typically imaged onto, or in direct contact with, the distal end of a fiber bundle. This image is transmitted to the proximal end of the bundle, from where it is relayed onto a sensor array, whose resolution is higher than the resolution of the fiber bundle (Fig. 2). This means that each fiber in the fiber bundle is mapped onto several sensors in the sensor array such that individual fibers, and the gaps between them, are visible in the recorded image. Each fiber in the bundle incurs a high blur on the part of the image that it transmits and the corresponding sensors in the sensor array all see a washed out highly blurred spot that effectively produces the same value on these sensors. Thus, each

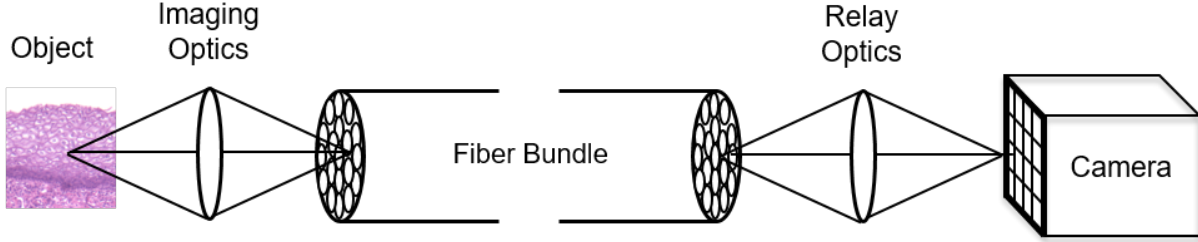


Figure 2. Diagram of a typical setup for traditional fiber bundle-based imaging.

fiber can be considered as one point/pixel in the observation. An example of this is shown in Fig. 1 where one can clearly see the loss in resolution due to imaging through a fiber bundle. Our objective in this paper is to improve the achievable resolution of a traditional fiber-bundle imaging setup.

2.1 Proposed architecture

To overcome the resolution limitation inherent to fiber bundles, we draw our attention towards CS-based computational imaging. Similar to the fiber bundle imaging setup, in conventional imaging, an object is typically imaged onto a low-resolution sensor array. However, CS-based computational imaging enables one to reconstruct a high resolution object by placing a mask in the imaging path (Fig. 3a). By taking several low resolution observations of the object, where each observation manipulates the object’s intensity or phase in a certain manner, one can reconstruct the object through numerical reconstruction algorithms that exploit the fact real-world images tend to have sparse representations in appropriate bases.²⁻⁶ The main difference is that while the resolution of the observations in (CS-based) computational imaging is limited by the spacing of individual sensors in the sensor array, the resolution of the observations in a fiber-bundle imaging setup is restricted by the spacing of individual fibers in the fiber bundle. Nonetheless, the concepts of computational imaging are transferable to the fiber-bundle imaging setup with appropriate modifications. Specifically, the setup in Fig. 2 can be modified to include a mask at a conjugate-image plane between the object and the bundle (Fig. 3b), and the mathematical model for Fig. 3a can be updated to include the addition of a fiber bundle in the imaging path. It is important to point out here that as the resolution of the fiber bundle is typically lower than the sensor array, the inherent reconstruction problem that one has to solve for a fiber-bundle imaging setup is computationally harder than traditional computational imaging.

We now discuss the specific details of our proposed architecture. The two key aspects that we considered when developing the computational imaging architecture for fiber-bundle-based imaging were: (i) the choice of imaging architecture, and (ii) the mapping of mask elements to individual fibers in the fiber bundle. For choosing the architecture in our setup, we must consider the nature of modulation (intensity, phase, etc.) and the location of the mask that best suits a fiber-bundle-based imaging system. Since endoscopic imaging is typically done in reflectance mode or with fluorescence, where light coming from tissue is spatially incoherent, architectures that use phase modulation are not feasible as they are more appropriate for spatially coherent light situations.¹⁷ In terms of the location of the mask in CS systems, it is mostly placed at a conjugate-image plane to spatially modulate the object’s intensity. Furthermore, we have previously shown that magnitude-only masks are more effective when used at a conjugate-image plane than at a conjugate-Fourier plane in a CS architecture.¹⁸ Therefore, we chose to build on previous work by integrating a mask into the fiber-bundle imaging system at a conjugate-image plane as depicted in Fig. 3b. We constructed an experimental platform based on Fig. 3b that uses a digital micromirror device (DMD) to simulate the projection of the object onto the mask (Fig. 3c). Typically, a DMD is used as a reprogrammable mask to obtain diverse observations in image-plane coded setups. However, in our experimental setup, we use it to display the mask overlaid with the object as illustrated in Fig. 3c, hence the term synthetic object. In the system, the DMD is imaged onto the front end of an oversized fiber bundle via the projection optics (Thorlabs AC254-100-A, then Thorlabs AC254-080-A). The back end of the bundle is then imaged onto a camera (Point Grey Research, GRAS-14S5M-C) via relay optics (Thorlabs AC254-30-A, then Thorlabs AC254-040-A). This concludes the description of our physical experimental platform.

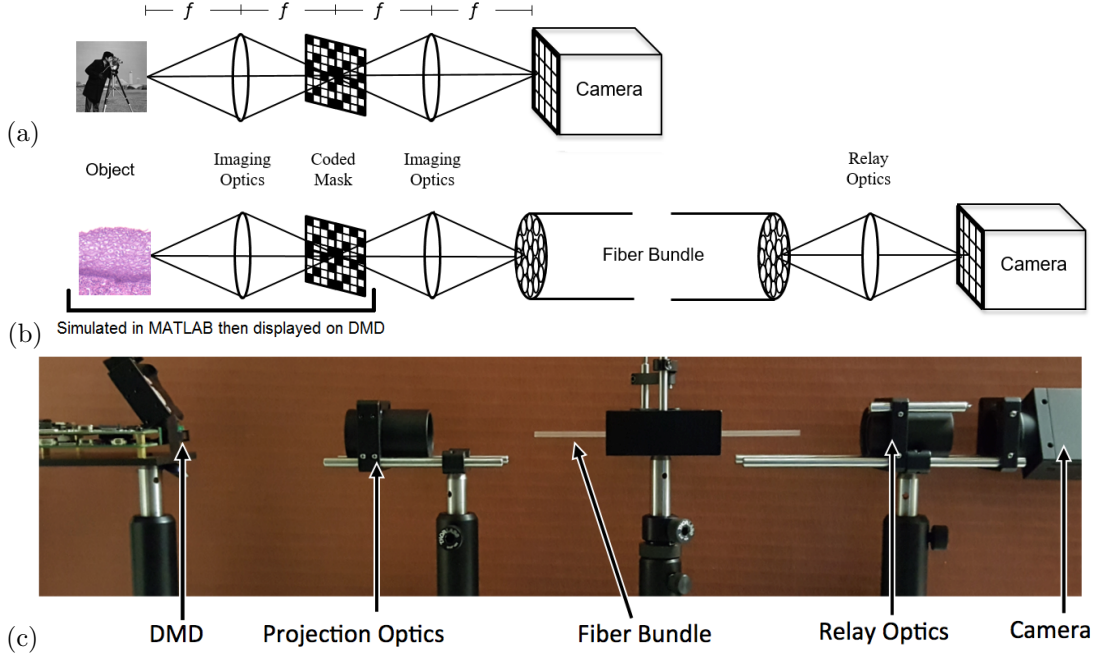


Figure 3. This figure makes a comparison between the architectures of traditional image-plane computational imaging and computational imaging through fiber bundles. (a) shows the traditional image-plane architecture for computational imaging. (b) is the image-plane architecture for imaging through fiber bundles. (c) shows our experimental setup for imaging through fiber bundles.

The second key aspect that we address in our architecture design is the element mapping from mask elements, in our case DMD elements, to the fibers in the bundle. In typical computational imaging systems, the modules (mask, imaging optics, sensor array, etc.) are aligned in a way that an integer downsampling is maintained from the mask elements to the sensors in the sensor array. In particular, each non-overlapping $d \times d$ square block from the mask is mapped onto a single sensor in the sensor array and this mapping holds for all sensors. Here d takes integer values and is referred to as the downsampling factor. In contrast, in a fiber-bundle based imaging system, several mask elements map onto a single, typically circular, fiber in the bundle. In addition, the fibers in a bundle are of different radii as well. These two constraints make it impractical to have a global integer downsampling factor when imaging through a fiber bundle. We will address this issue of element mapping for fiber-bundle imaging in the forthcoming sections.

We conclude this section by pointing out that, as can be seen in Fig. 1, there are opaque gaps between the individual fibers in the fiber bundle due to the epoxy/cladding that holds fibers together. The part of our object imaged onto these gaps does not appear in the observations and hence cannot be recovered through CS reconstruction algorithms. This limitation in fiber-bundle imaging lies outside the scope of this paper and will be explored in future publications.

3. FORWARD MODEL OF COMPUTATIONAL IMAGING THROUGH A FIBER BUNDLE

As discussed in the previous section, although many possible CS-based computational imaging architectures exist, we focus on a system that uses lenses to image an object through an image-plane mask. Specifically, we use a $4f$ imaging architecture with intensity masks placed at a conjugate-image plane (see Fig. 3a). Note that while we are focused on spatially incoherent illumination, this image-plane setup results in the same forward model for spatially coherent illumination strategies. Readers interested in the details of the coherent and incoherent systems unexplored in this paper can refer to the relevant publications.^{17, 19, 20}

3.1 Image-plane coding architecture

For a 4f image-plane coding architecture, the modulation agent, i.e., the mask, is situated at a conjugate image plane between the object and the sensor to modulate the intensity being observed on the sensor end. This architecture is shown in Fig. 3a. Denoting the imaged object as \mathbf{X} , the $n \times n$ mask as \mathbf{M} and the $m \times m$ observations as \mathbf{Y} where $m \ll n$, we can write the following equation for observed image:⁸

$$\mathbf{Y} = \mathbf{D}_r \{ \mathbf{h} * [\mathbf{M} \odot \mathbf{X}] \} \mathbf{D}_c \quad (1)$$

where \odot denotes the Hadamard product, $*$ represents the 2-D convolution operation, \mathbf{h} is a system specific convolution kernel that models the contributions and mappings from mask elements to sensor elements, and \mathbf{D}_r and \mathbf{D}_c represent the $m \times n$ and $n \times m$ downsampling in the rows and columns, respectively. A noteworthy point is that the achievable resolution in the reconstructed image is limited by the resolution of the mask. We can rewrite the observation model (1) in vector form, as presented in the following equation:

$$\mathbf{y} = \mathbf{D} \mathbf{T}_h \bar{\mathbf{M}} \mathbf{x} \quad (2)$$

where \mathbf{y} is the $m^2 \times 1$ vectorized observation, \mathbf{x} is the $n^2 \times 1$ vectorized object, $\bar{\mathbf{M}}$ is a $n^2 \times n^2$ diagonal matrix with mask elements on the diagonal, \mathbf{T}_h is a block Toeplitz convolution matrix obtained from \mathbf{h} , and \mathbf{D} denotes the appropriate downsampling operation (combining downsampling in both directions). All of this manipulation is done to bring our system into the much recognized system model, $\mathbf{y} = \mathbf{A} \mathbf{x}$, used in CS literature. Here $\mathbf{A} = \mathbf{D} \mathbf{T}_h \bar{\mathbf{M}}$ denotes the measurement/sensing matrix, which is completely dependent on the system and highly impacts the quality of reconstructions. In most cases, for computational imaging, one observation is insufficient to reconstruct \mathbf{x} from \mathbf{y} using CS-reconstruction methods. Thus several observations are used, each with a different mask, to obtain a larger system of equations that provides better reconstruction. To this end, denoting the matrix for the i -th mask as $\bar{\mathbf{M}}_i$ and the i -th observation as \mathbf{y}_i , the actual system of equations in consideration can be written as:

$$\begin{bmatrix} \mathbf{y}_1 \\ \mathbf{y}_2 \\ \vdots \\ \mathbf{y}_K \end{bmatrix} = \begin{bmatrix} \mathbf{D} \mathbf{T}_h \bar{\mathbf{M}}_1 \\ \mathbf{D} \mathbf{T}_h \bar{\mathbf{M}}_2 \\ \vdots \\ \mathbf{D} \mathbf{T}_h \bar{\mathbf{M}}_K \end{bmatrix} \mathbf{x} \quad (3)$$

where K is the total number of observations. For this larger system, the measurement matrix is the concatenation of all of the individual measurement matrices.

3.2 Fiber-optic image-plane architecture

We can now formulate the forward model for our proposed computational endomicroscopy architecture. A graphical representation of this architecture can be seen in Fig. 3b. The only change from a standard image-plane architecture (Fig. 3a) is at the sensor-end where the light first passes through the fiber bundle before falling onto the sensor array. Since each fiber is mapped to multiple sensors on our sensor array, all of these sensors can be effectively considered as one observation pixel by adding their individual values. This changes our forward model from the standard image-plane forward model as follows:

$$\mathbf{Y} = \mathbf{D}_f (\mathbf{F} \odot (\mathbf{D}_r \{ \mathbf{h} * [\mathbf{M} \odot \mathbf{X}] \} \mathbf{D}_c)) \quad (4)$$

where \mathbf{F} represents the transmissivity of the fibers in the bundle and $\mathbf{D}_f(\cdot)$ represents a function that defines the mapping of mask elements to the fibers in the bundle. The matrix \mathbf{F} can be obtained from the system when the bundle is illuminated in the absence of object and mask. This image can also be used to construct $\mathbf{D}_f(\cdot)$. The representation in (4) can be represented in a much simpler way for a vector representation of this architecture (as done previously for standard image-plane architecture):

$$\mathbf{y} = \mathbf{D}_F \bar{\mathbf{F}} \mathbf{D} \mathbf{T}_h \bar{\mathbf{M}} \mathbf{x} \quad (5)$$

where $\bar{\mathbf{F}}$ is a diagonal matrix with the entries of \mathbf{F} on its diagonal, and \mathbf{D}_F is now a binary $\{0, 1\}$ matrix that defines the mapping of mask elements to the fibers in the bundle. To construct \mathbf{D}_F , we can use the image \mathbf{F} of the bundle from our system and perform circle detection to find the centers and radii of the fibers. With the centers and radii of the fibers in the bundle, we can easily make \mathbf{D}_F to map mask elements to the fibers. This can be done using any off-the-shelf circle detection algorithm with appropriately tuned parameters. The number of rows in \mathbf{D}_F is equal to the number of fibers in the bundle and the number of nonzero entries in a row of \mathbf{D}_F equals the number of mask elements mapped onto that respective fiber. Thus, the measurement matrix \mathbf{A} for our proposed architecture can be written as $\mathbf{A} = \mathbf{D}_F \bar{\mathbf{F}} \mathbf{D} \mathbf{T}_h \bar{\mathbf{M}} \mathbf{x}$.

Recall that the fiber bundle has gaps between individual fibers that are opaque. This means that the part of our imaging object falling on this gap is lost and we can only recover parts of our object that fall on the fibers. Nonetheless, we can combine multiple observations, as we did in (3), to make a system of equations that is solvable through CS reconstruction algorithms.

3.3 Optical imperfections

The aforementioned forward model for our proposed fiber bundle-based computational imaging setup represents the ideal case scenario. In the ideal case, the system specific convolution kernel \mathbf{h} is a matrix that denotes the contributions from just the mask elements that map onto a fiber. However, in case of inevitable optical imperfections in the system, \mathbf{h} is usually a larger matrix and models the mapping imperfections and contributions from neighboring mask elements to individual fibers.⁸ This larger kernel associated with the system can be learned by using observations from known (training) images and then using non-negative least squares to solve for \mathbf{h} from the following linear system:

$$\mathbf{y} = \mathbf{D}_F \bar{\mathbf{F}} \mathbf{D} \mathbf{T}_{\bar{\mathbf{M}}} \mathbf{h} \quad (6)$$

where $\mathbf{T}_{\bar{\mathbf{M}}}$ is now the block Toeplitz convolution matrix obtained from $\bar{\mathbf{M}} \mathbf{x}$.

4. SIMULATED SETUP

We now move on to the numerical simulations of our proposed architecture and model for fiber bundle-based computational imaging. We provide results for two scenarios: one where the true convolution kernel is known and the other where it is unknown. In the case where the true kernel is unknown, we use some predefined kernel for reconstruction. For all simulations in this section, the masks were of size 256×256 , which is also the size of the reconstructed images. Each mask was generated as a random matrix with integer elements drawn uniformly at random in the range $[0, 255]$. The true kernel in all simulations was an 8×8 Gaussian low pass kernel with standard deviation 1.75.

4.1 Known convolution kernel

For our first set of simulations, we assume the model with optical imperfections. However, we also assume access to the true kernel \mathbf{h} modeling these imperfections. We consider two different objects for imaging: one is a cropped 1951 USAF resolution target image (Fig. 4d) and the other is the popular cameraman image (Fig. 4h). Moreover, we consider two arrangements of the fibers in the fiber bundle. The first one has a simple pattern which we refer to as the regular fiber grid (Fig. 4a). The second arrangement with misaligned fibers is referred to as the irregular fiber grid (Fig. 5a) and is more representative of an actual fiber bundle.

Fig. 4 shows results for reconstruction of the two objects for the case of the regular fiber grid. The results of reconstructions with varying number of observations are shown in Fig. 4e–Fig. 4g (target image) and Fig. 4i–Fig. 4k (cameraman image). Comparing the reconstructions with the no mask observation (Fig. 4b and Fig. 4c) from the setup (which is what a typical observation from a traditional fiber-bundle imaging setup would look like), we do not see an immediate improvement. However, as we keep increasing the number of observations used for reconstruction, we successively resolve more features in the reconstructed image.

Fig. 5 shows reconstruction results for just the cameraman image for the case of the irregular fiber pattern. Once again, we observe that computational imaging results in better spatial resolution than traditional fiber-bundle imaging. From the reconstruction in Fig. 5, we can see that increasing the number of observations improves

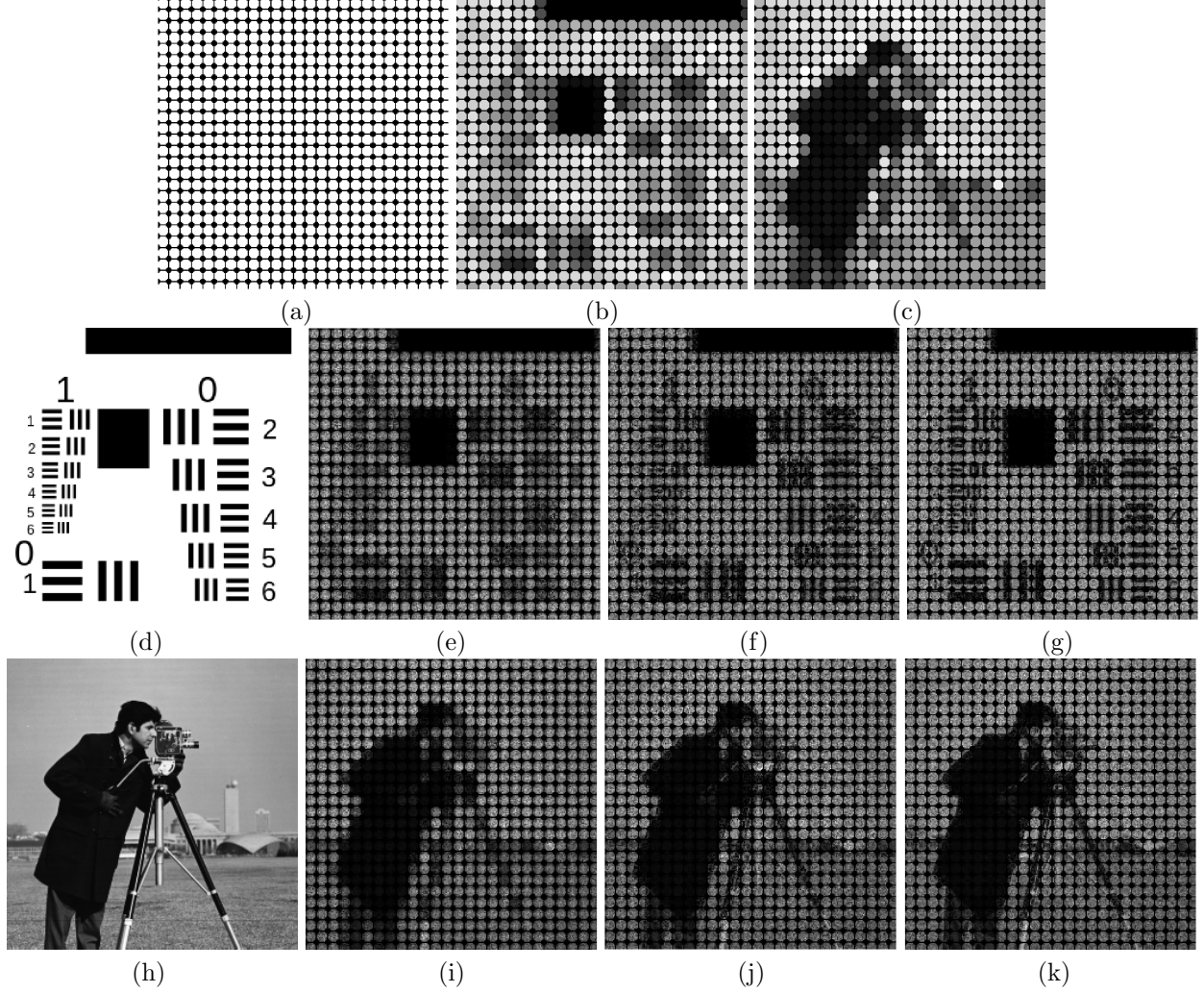


Figure 4. This figure shows the results from simulations for imaging of two different objects through a fiber bundle-based computational imaging system with a regular grid pattern and known convolution kernel. (a) depicts the ideal/regular fiber pattern used for these simulations. (b) and (c) show examples of observations through the fiber bundle without any mask for the two objects in consideration. (d) shows the cropped target image used as the first object. (e), (f) and (g) show reconstructions using 10, 50 and 100 observations, respectively, for the target image. (h) is the cameraman image used as the other object. (i), (j) and (k) have the reconstructions using 10, 50 and 100 observations, respectively, for the cameraman image.

the resolution. This is encouraging because the physical fiber bundles rarely have an ideal grid arrangement of fibers. Finally, Fig. 5 also shows that resolution of the reconstructed image in the case of irregular fiber pattern also increases with an increase in the number of observations.

4.2 Unknown convolution kernel

Next, we perform numerical experiments under the assumption of an unknown convolution kernel. In this case, we use a predefined convolution kernel instead of the true kernel. This predefined kernel is a $d \times d$ matrix with all entries equal to $1/d^2$, where d is the mode of all radii values for the fibers in the bundle. We will only focus on the irregular grid of fiber pattern and the target image in these simulations. We can see from Fig. 6 that the reconstructions with the incorrect kernel are inferior to the reconstructions with the true kernel. However, the encouraging observation is that we are still able to reconstruct some larger features (Group-0 features in Fig. 6c) even in this case.

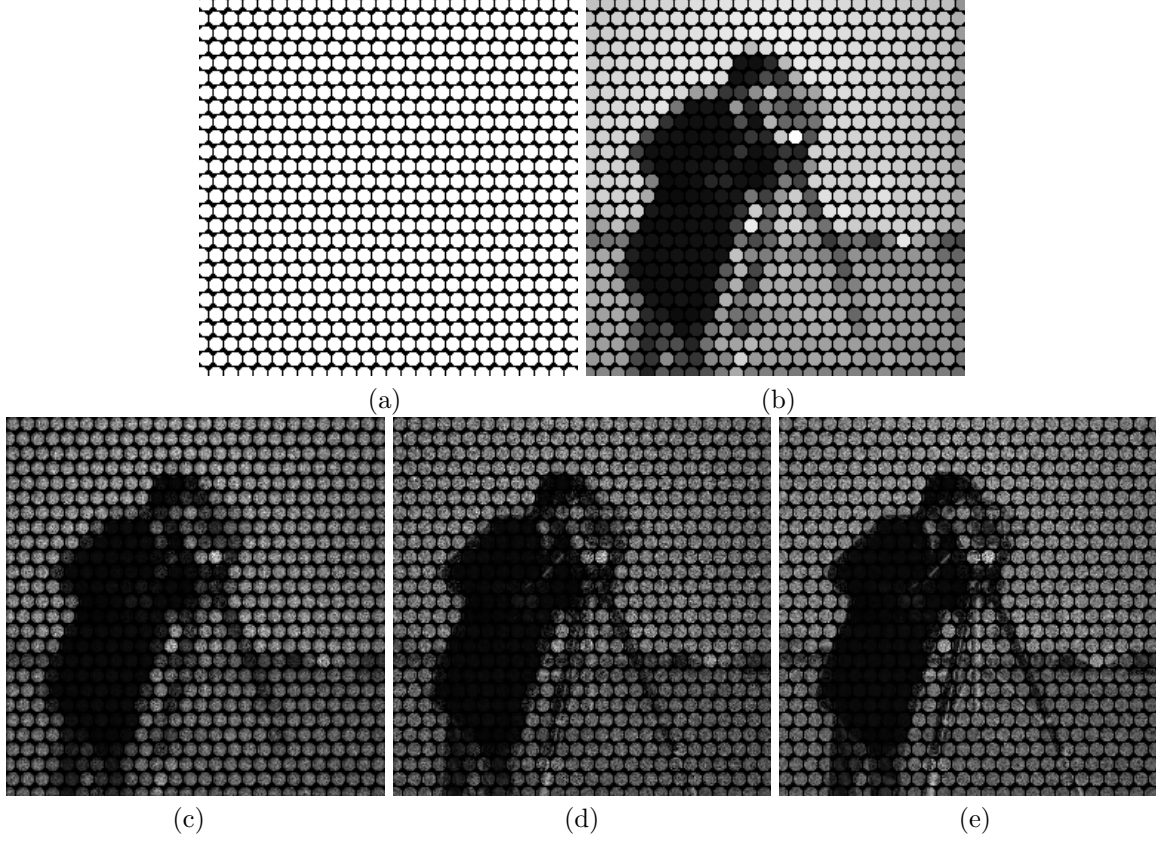


Figure 5. This figure shows the results from simulations for imaging of the cameraman image through a fiber bundle-based computational imaging system with irregular grid pattern and known convolution kernel. (a) depicts the irregular fiber pattern used for these simulations. (b) shows an observation through the fiber-bundle without any mask. (c), (d) and (e) have the reconstructions using 10, 50 and 100 observations, respectively, for the cameraman image.

4.3 Effect of fiber radii and bin factor of masks

Next, we investigate the effect of fiber radii and the size of mask elements on the reconstructions by running simulations for fibers of radii 5 and 11 units. Here we define the radii in terms of the mask elements; e.g., a radius of 5 means that an individual fiber has 5 mask elements contained within its radius. Note also that, for a fiber of particular radius, we can use the coded mask in several ways. Specifically, we could assign different random values to different mask elements or we could make $d \times d$ groups of mask elements and assign random values to these groups. We term the latter setup as *binning* and we define d to be the bin factor. In Fig. 7, we show reconstructions of the target image for fibers of radii 5 (2nd row) and 11 (3rd row), and masks with bin factors $d = [1, 2, 4, 8]$, where $d = 1$ means no binning.

The first observation we make from Fig. 7 is that fibers of smaller radii result in better reconstructions. This seems logical as the bundle with smaller fibers has more fibers in a given area, which gives us more points/pixels in our final observations. The second observation is the relation between mask binning, fiber radius, and reconstruction quality. For the fibers of radius 5, the best reconstructions are with masks that have a bin factor of $d = 2$ (Fig. 7e). On the other hand, masks with bin factor of $d = 4$ (Fig. 7j) produce the best reconstruction for fibers with radius 11. This suggests that as the fiber radius increases, one will benefit from using masks with larger bin factors. But one must also be cautious about choosing the appropriate bin factors as masks with too large bin factors result in poor reconstructions (Fig. 7g).

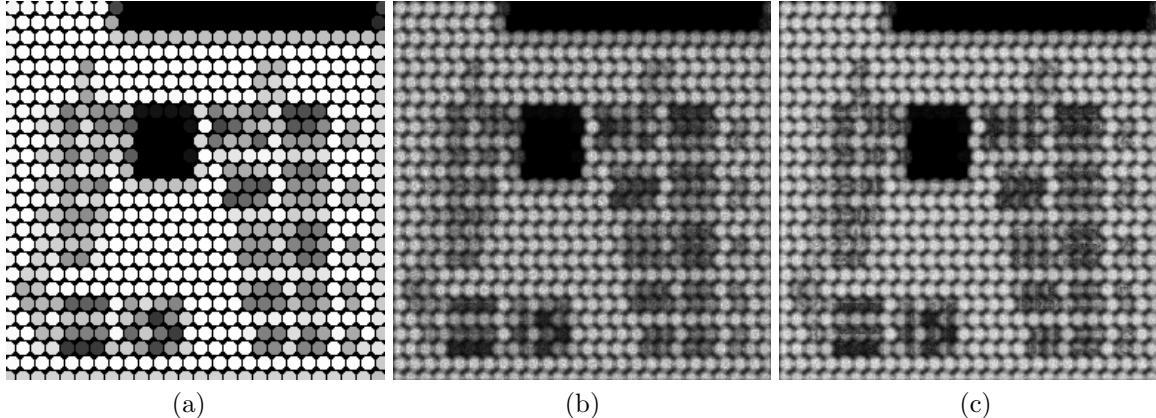


Figure 6. This figure shows the results from simulations for imaging of the USAF target image through a fiber bundle-based computational imaging system with irregular grid pattern and unknown convolution kernel. (a) shows the no mask observation through the fiber bundle. (b) and (c) show the reconstructions using 50 and 100 observations, respectively.

5. EXPERIMENTAL SETUP

Next we look at the reconstructions from our experimental platform using a synthetic object. This is done initially as a proof of concept experiment to show that methods discussed in the previous section can be translated to a hardware implementation. For simplicity, we are imaging synthetic objects, but the experimental platform can be modified to image real objects by projecting a scene onto the DMD. The synthetic object used in these experiments was a custom designed image of size 200×200 with line pairs of varying width. Further, the masks used in these experiments were of the same size as well, i.e., 200×200 . At the back end, we gathered the values from each individual fiber to obtain one observation point per fiber in post-processing. Finally, we reconstructed images of size 200×200 with varying numbers of observations. The results are shown in Fig. 8. We can see from the figures that we are able to resolve some features in the reconstructed images that are not present in no mask observation. Further experiments that compare different fiber radii and mask types are left as the subject of future investigation.

6. CONCLUSION

This paper introduced a new setup that integrates compressive sensing (CS) principles into endoscopy imaging. This was achieved by the introduction of a mask at the conjugate image plane in the imaging path of a fiber bundle-based imaging system. The forward model for this modified imaging setup was formulated and tested through both simulations and experimental data. The results suggested that CS-based endoscopy imaging is likely to have superior resolution compared to traditional endoscopy imaging. Future work in this regard will focus on imaging with real-world data and tissue samples, accounting for the opaque regions in the imaging path, and estimating the true convolution kernel using training images.

ACKNOWLEDGMENTS

This work was supported in part by the National Science Foundation under grants CCF-1453073 and ECCS-1509260, and by the Army Research Office under grant W911NF-14-1-0295.

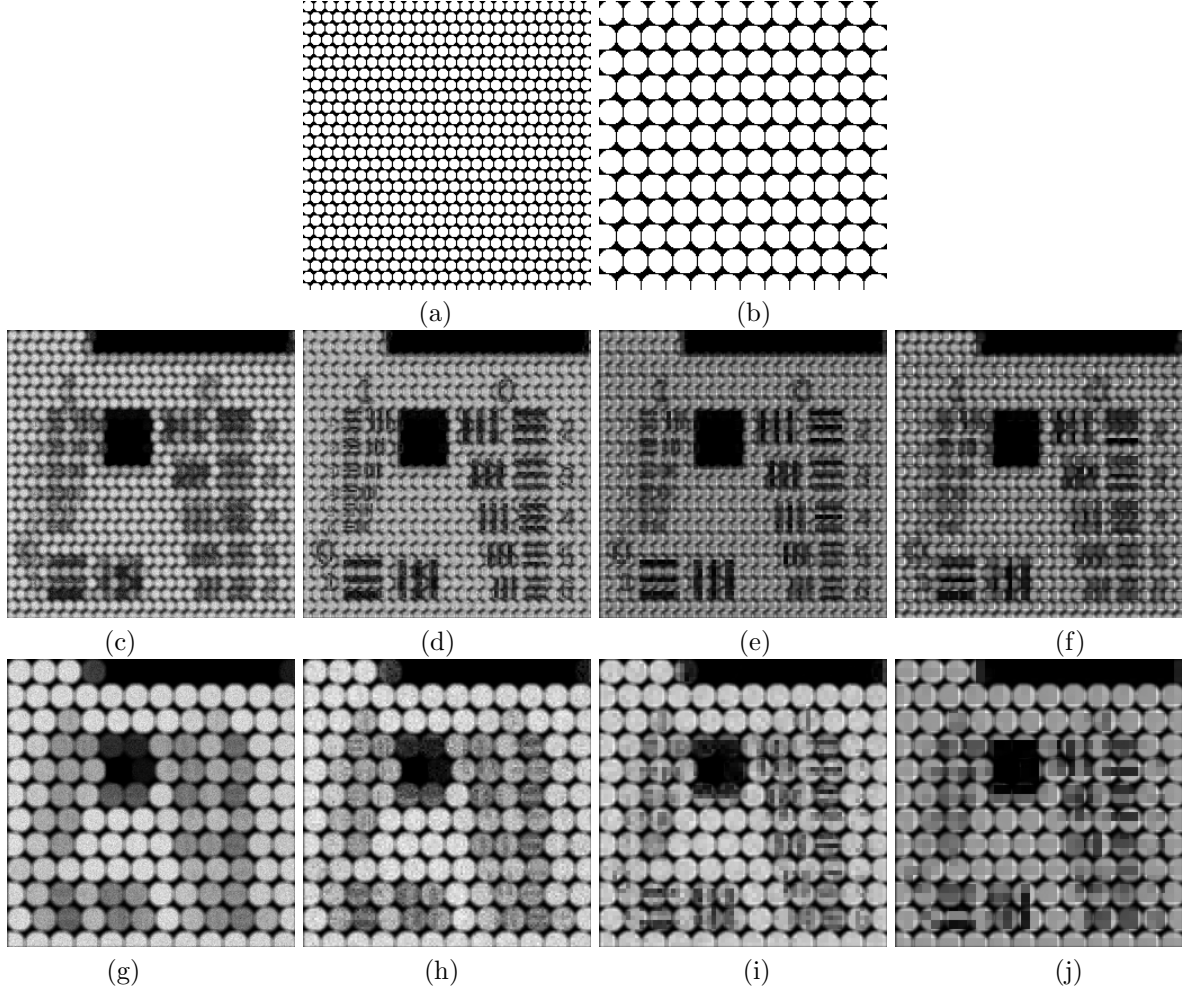


Figure 7. This figure makes a comparison of the trade-off between the reconstruction quality, fiber radii and the bin factor of the masks. (a) and (b), respectively, show the fiber bundles with radii 5 and 11 used for these simulations. (c), (d), (e) and (f) show reconstructions for a fiber bundle with radius 5 (all with 100 observations) for masks with bin factors $d = [1, 2, 4, 8]$, respectively. Similarly, (g), (h), (i) and (j) show same reconstructions for a fiber bundle with the radius 11. All simulations here are done *without* the knowledge of the true kernel.

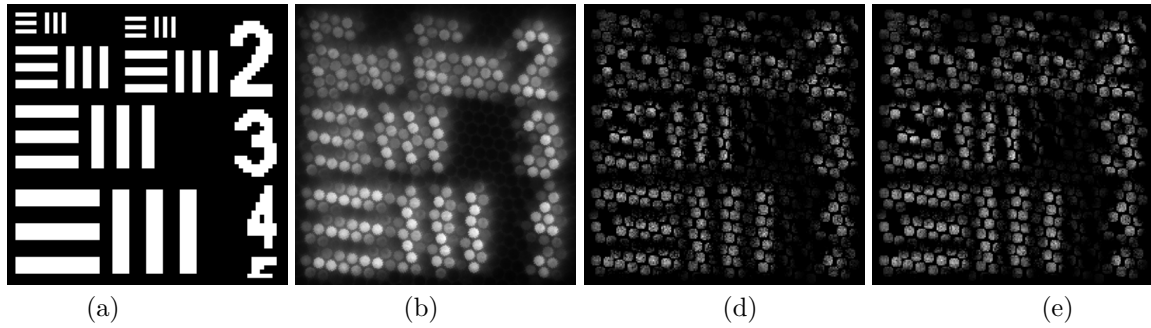


Figure 8. This figure shows results for the simulated data from the experimental setup. (a) shows the original image for reference. (b) shows the no mask image seen by the camera. (c) and (d) show reconstructions with 50 and 100 observations, respectively.

REFERENCES

- [1] Chen, X., Reichenbach, K. L., and Xu, C., “Experimental and theoretical analysis of core-to-core coupling on fiber bundle imaging,” *Optics express* **16**(26), 21598–21607 (2008).
- [2] Candès, E. J. et al., “Compressive sampling,” *Proc. Int. Congr. Math.* **3**, 1433–1452 (2006).
- [3] Candès, E. J., Romberg, J., and Tao, T., “Robust uncertainty principles: Exact signal reconstruction from highly incomplete frequency information,” *IEEE Trans. Inf. Theory* **52**, 489–509 (2006).
- [4] Candès, E. J., Romberg, J. K., and Tao, T., “Stable signal recovery from incomplete and inaccurate measurements,” *Commun. Pure Appl. Math.* **59**, 1207–1223 (2006).
- [5] Candès, E. J. and Tao, T., “Near-optimal signal recovery from random projections: Universal encoding strategies?,” *IEEE Trans. Inf. Theory* **52**, 5406–5425 (2006).
- [6] Donoho, D. L., “Compressed sensing,” *IEEE Trans. Inf. Theory* **52**, 1289–1306 (2006).
- [7] Duarte, M. F., Davenport, M. A., Takbar, D., Laska, J. N., Sun, T., Kelly, K. F., and Baraniuk, R. G., “Single-pixel imaging via compressive sampling,” *IEEE Signal Process. Magazine* **25**(2), 83–91 (2008).
- [8] Dumas, J. P., Lodhi, M. A., Bajwa, W. U., and Pierce, M. C., “Computational imaging with a highly parallel image-plane-coded architecture: challenges and solutions,” *Optics express* **24**(6), 6145–6155 (2016).
- [9] Shepard, R. H., Fernandez-Cull, C., Raskar, R., Shi, B., Barsi, C., and Zhao, H., “Optical design and characterization of an advanced computational imaging system,” in [*SPIE Optical Engineering + Applications*], 92160A–92160A, International Society for Optics and Photonics (2014).
- [10] Ke, J. and Lam, E. Y., “Object reconstruction in block-based compressive imaging,” *Optics express* **20**(20), 22102–22117 (2012).
- [11] Chen, H., Salman Asif, M., Sankaranarayanan, A. C., and Veeraraghavan, A., “FPA-CS: Focal plane array-based compressive imaging in short-wave infrared,” in [*Proc. of IEEE Conf. Comp. Vision Patt. Recog.*], 2358–2366 (2015).
- [12] Arguello, H. and Arce, G. R., “Colored coded aperture design by concentration of measure in compressive spectral imaging,” *IEEE Trans. Image Processing* **23**(4), 1896–1908 (2014).
- [13] Galvis, L., Arguello, H., and Arce, G. R., “Coded aperture design in mismatched compressive spectral imaging,” *Applied optics* **54**(33), 9875–9882 (2015).
- [14] Arguello, H., Rueda, H., Wu, Y., Prather, D. W., and Arce, G. R., “Higher-order computational model for coded aperture spectral imaging,” *Applied optics* **52**(10), D12–D21 (2013).
- [15] Dong, S., Nanda, P., Shiradkar, R., Guo, K., and Zheng, G., “High-resolution fluorescence imaging via pattern-illuminated fourier ptychography,” *Optics express* **22**(17), 20856–20870 (2014).
- [16] Tian, L., Li, X., Ramchandran, K., and Waller, L., “Multiplexed coded illumination for fourier ptychography with an LED array microscope,” *Biomedical optics express* **5**(7), 2376–2389 (2014).
- [17] Willett, R. M., Marcia, R. F., and Nichols, J. M., “Compressed sensing for practical optical imaging systems: a tutorial,” *Optical Engineering* **50**(7), 072601–072601 (2011).
- [18] Dumas, J. P., Lodhi, M. A., Bajwa, W. U., and Pierce, M. C., “Evaluation of computational endomicroscopy architectures for minimally-invasive optical biopsy,” in [*Proc. of SPIE*], **10040**, 1004006–1 (2017).
- [19] Goodman, J. W., [*Introduction to Fourier optics*], Roberts and Company Publishers (2005).
- [20] Voelz, D. G., [*Computational fourier optics: A MATLAB tutorial*], SPIE Press Bellingham, WA (2011).